A Metal-Organic Framework as Fluorescent and Colorimetric Dual-Signal Readout Biosensor Platform for the Detection of a Genetic Sequence from the SARS-CoV-2 Genome

John C. Hadynski[1], Jaren Diggins[2], Zachary Goad[1], Monu Joy[1], Steven Dunckel[1], Petra Kraus[3], Thomas Lufkin[3], Mario Wriedt[1*]

[1] Department of Chemistry & Biomolecular Science, Clarkson University, Potsdam, New York 13699, United States.

[2] Department of Chemistry, Texas Southern University, Houston, Texas, 77004, United States.

[3] Department of Biology, Clarkson University, Potsdam, New York 13699, United States.

* Corresponding author: mwriedt@clarkson.edu

Abstract

The quest for the development of high-accuracy, point-of-care, and cost-effective testing platforms for SARS-CoV-2 infections is ongoing as current diagnostics rely on either assays based on costly yet accurate nucleic acid amplification tests (NAAT) or less selective and less sensitive but rapid and cost-effective antigen tests. As a potential solution, this work presents a fluorescence-based detection platform using a metal-organic framework (MOF) in an effective assay, demonstrating the potential of MOFs to recognize specific targets of the SARS-CoV-2 genome with high accuracy and rapid process turnaround time. As a highlight of this work, positive detection of SARS-CoV-2 is indicated by a visible color change of the MOF probe with ultra-high detection selectivities down to single-base mismatch nucleotide sequences, thereby providing an alternative avenue for the development of innovative detection methods for diverse viral genomes.

Keywords: Metal-organic framework, SARS-CoV-2, Biosensor, dual-signal readout, DNA/RNA detection

Introduction

The novel SARS-CoV-2 coronavirus is the causative agent of COVID-19, a respiratory disease that exhibits a wide range of clinical outcomes from mild disease to severe pneumonia and acute respiratory distress syndrome which can result in death. SARS-CoV-2 can spread efficiently from person-to-person; its world-wide outbreak was classified as a pandemic by the World Health Organization (WHO) in March 2020.[1–3]

While vaccination is the most effective defense against serious illness related to the infection, testing for active infections, and isolating those individuals who test positive have been determined by the WHO as one of the most effective means to contain the further spread of COVID-19.[4] Expediting such measures is strongly tied to the availability of reliable and cost-effective diagnostics to test thousands of symptomatic and asymptomatic patients daily.[5]

FDA-approved diagnostics for active infections are currently limited to (i) nucleic acid amplification tests (NAAT) which amplify and detect RNA fragments of the SARS-CoV-2 genome[6], and (ii) antigen-based methods which detect characteristic proteins of the SARS-CoV-2 virus[7,8]. Among NAAT methods, reverse transcription-polymerase chain reaction (RT-PCR)[9,10] and reverse transcription loop-mediated isothermal amplification (RT-LAMP)[11] are the most prominent diagnostics employed today. Both methods feature high detection sensitivities, but they are plagued by requiring expensive instrumentation. In addition, RT-PCR comprises a lengthy amplification process (several hours) including the need to transport samples to specialized laboratories, while RT-LAMP is point-of-care appropriate and features rapid amplification (minutes).[12,13] In contrast, antigen diagnostic kits are highly cost-effective since they require no instrumentation for implementation and also feature point-of-care implementation and exhibit rapid detection. However, they are less sensitive and less accurate in comparison to NAAT methods.[8,14,15] This dilemma motivates quests for the development of testing methods marrying cost-effectiveness with reliability including increased sensitivity, specificity, test simplicity, and decreased turnaround time. In addition, the ideal method should be scalable to avoid backlogs as commonly found for NAAT-based diagnostics during COVID-19 surges. Herein, we address this quest by employing a metal-organic framework (MOF) as a novel detection platform for SARS-CoV-2 which allows both point-of-care testing as well as molecular-genetic level accuracy.

Over the past two decades, MOFs have emerged as a new class of nanoporous materials composed of metal ions or clusters interconnected by polytopic organic linkers that form multi-dimensional crystalline networks. Their resulting topologies, pore environments, and functionalities are controllable by both the choice of metal and organic building blocks.[16] Key features—large accessible voids and high internal surface areas—render MOFs as ideal candidates for adsorption-based applications,[17] while the potential to functionalize their pore environments and tune their topologies and pore sizes offers applications such as detection platforms for numerous molecular species.[18] In this context, perhaps the most important yet least explored analytes to date are biomolecules (e.g., proteins, nucleic acids and antibodies).[19] While fluorescence sensing is a well-established strategy to detect RNA in other settings[20], MOFs represent a new technological platform not yet exploited clinically. A few MOF studies have investigated the detection of RNA targets from viral genomes of Ebola virus,[21,22] Human Immunodeficiency virus 1,[23,24] Sudan virus,[24,25] Dengue virus,[26] and Zika virus,[26] but studies on SARS-CoV-2 have not yet been conducted given the

infancy of the infancy of studies related to RNA detection in the MOF field. Noteworthy though, the potential use of MOFs as COVID-19 assay has been widely discussed within the current literature over the past couple of years,[27–32] including a few recent reports on the detection of specific COVID-19 biomarkers,[33–37] but to the best of our knowledge, we are first to report on the experimental implementation of genetic SARS-CoV-2 detection.

Results and Discussion

Detection strategy design. Our detection strategy follows a sophisticated process as represented in **Figure 1**. In brief, a fluorophore-labeled (FL) single-stranded DNA oligonucleotide, complementary to a unique RNA sequence of the SARS-CoV-2 genome (denoted here as "probe ssDNA" or "P-DNA") is adsorbed into a porous MOF matrix with the resulting P-DNA@MOF system serving as the sensing platform for SARS-CoV-2 RNA. Within this platform, strong non-covalent intermolecular P-DNA—MOF interactions result into fluorescence quenching (signal off) of the FL tag. The prevalent quenching mechanism likely processes *via* photoinduced electron-transfer (PET) since fluorescence resonance energy transfer (FRET) can be excluded as mechanism as evidenced from lack of visible light absorption of the pristine MOF.[38] **Figure S1** shows the respective diffuse reflectance data of the MOF. For RNA detection, stable RNA–P-DNA hybrid duplexes are formed upon adding viral RNA targets that are complementary to the P-DNA sequence of the P-DNA@MOF platform. This duplex formation significantly decreases the P-DNA–MOF affinity due to the absence of unpaired nucleotides resulting from strong RNA–P-DNA interactions. As a direct result, fluorescence regeneration of the FL tag (signal on) is observed, since the now more stable hybrid duplex has less affinity to the MOF and desorbs from the MOF pores. This change of fluorescent emission can be directly assessed by fluorescence spectroscopy. This methodology is inspired from previous work on MOF-based luminescence switch sensors and has been modified as detailed below[19].

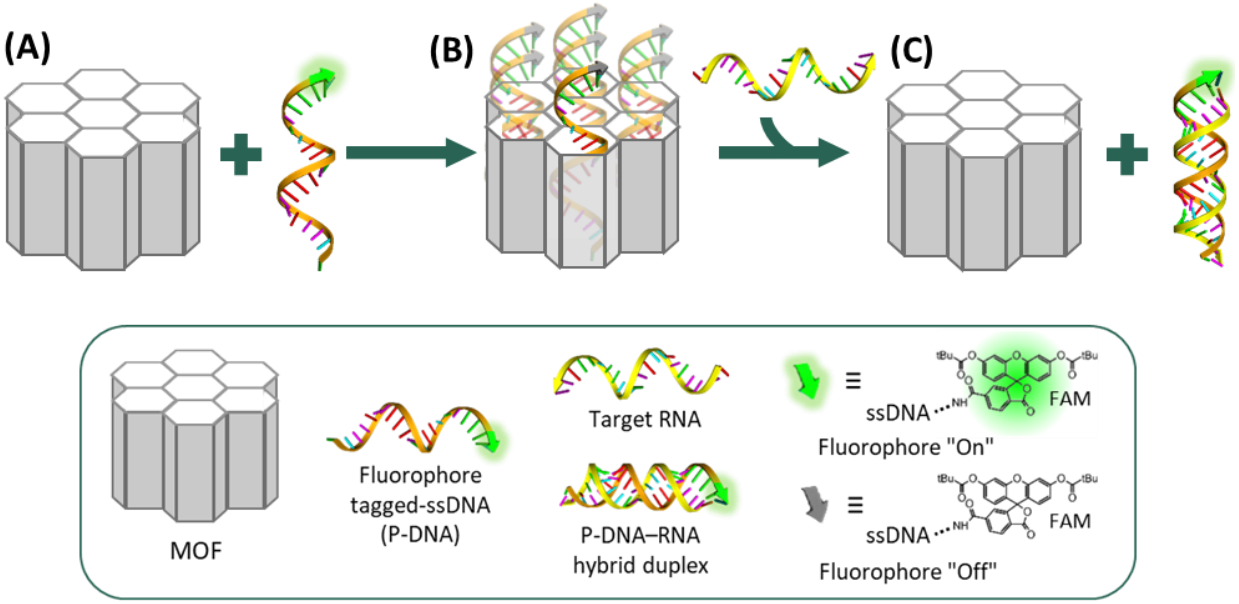

Figure 1. Schematic representation (not to scale) illustrating the fluorescence quenching-regeneration mechanism of viral RNA detection using a MOF-based sensing platform. Shown is the (A) empty MOF which adorbs P-DNAs to form (B) a P-DNA@MOF system resulting in fluorescence quenching of the P-DNA. (C) Upon target RNA binding, P-DNA–RNA hybrid duplexes are formed and ejected from the MOF pores resulting in fluorescence regeneration.

Probe selection, fabrication, and characterization. Based on our extensive prior experience in MOF incorporation of large molecular guest species[39–42] we identified five essential criteria to select candidate MOFs for the preparation of P-DNA@MOF platforms: (i) pore diameter should be >2.0-2.5 nm to accommodate adsorption of P-DNA and to enable RNA–P-DNA duplex formation within the MOF pore. This is a crucial requirement given that P-DNA and RNA–P-DNA duplexes possess kinetic diameters of approx. 2.0 nm as displayed in **Figure 2A**; (ii) pore geometry should feature 1D channels to accommodate 1D helical oligonucleotides; (iii) pore functionalities should enable defined noncovalent P-DNA–MOF interactions to induce PET processes for quenching of the fluorophore; (iv) MOF should be stable in water to sustain porosity and functionality under *in vitro* conditions using aqueous buffer media; and (v) MOF synthesis should have potential for scalability through simple and cost-effective synthetic routes.

Noteworthy, from the assessment of foundational work[27–29], we found that any MOF previously explored for RNA detection does not meet the pore size criteria. **Table S1** provides a comprehensive overview of respective pore diameters showing that those MOFs are either non-porous or exhibit pores <<2.0 nm. Therefore, informed from this structural analysis and contrary with the reported interpretations, one can exclude true P-DNA adsorption within the MOF pores and any pore-driven PET fluorescence quenching mechanisms in current literature. Instead, undefined MOF particle surface phenomena might

play a major role for the PET process, and thus, leaving the full potential of MOFs unexploited. This conclusion is supported by a recent study of Xiang Zhou *et al.*[43] in which they show that the limited pore size (1.5 nm) of Ni-MOF-74 does not facilitate P-DNA adsorption while the isoreticular series Ni-MOF-74-II-V with pore sizes ranging 2.2-4.2 nm show significant uptake. Evidenced by X-ray diffraction analysis, the entire nucleic acid chain was found completely confined inside the pores providing excellent protection. Inspired by this work but given the synthetic complexity of this Ni-MOF-74 series, we selected instead for the herein reported proof-of-concept study the mesoporous MOF MIP-206-R (R = Me) as the ideal candidate platform for P-DNA inclusion.[44] While this MOF exists in different isostructural variants (e.g., R = H, F, Br, OH, NH_2, SO_3H, OMe) we selected the methyl variant with the expectation that the non-polar and minimal-bulky nature of the methyl group is able to provide moderately strong non-specific interactions between the MOF and P-DNA. This MOF can be readily synthesized from a one-pot reaction in a solvothermal synthesis autoclave at 180 °C using the commercially available ligand 5-methylisophthalic acid (Me-IPA), zirconium(IV) chloride and formic acid as solvent. The crystal structure of MIP-206-Me consists of two types of Zr oxo-cluster secondary building units, namely 8-connected Zr_6 and 12-connected Zr_{12} oxo-clusters, which are bridged by Me-IPA ligands into a 3D porous architecture with accessible 1D meso-channels running along the *c* axis (**Figure 2B**). These channel pores are 2.6 nm in diameter and are decorated with aromatic functionalities, both of which constitutes an ideal environment for P-DNA immobilization and fluorophore quenching *via* PET. Also, evident from characterizations *via* powder X-ray diffraction (PXRD, **Figure 2C**) and scanning electron microscopy (SEM, **Figure S2**), this MOF shows excellent crystallinity with uniform particle sizes of aggregates around 100 nm and significant stability in water. The small particle size is expected to minimize diffusion limitation for P-DNA adsorption.

The P-DNA selection process was guided from CDC-approved sequences for current RT-PCR testing,[45] and it is expected that oligonucleotides with high guanine/cytosine (G/C) content (>50%) will aid the formation of stable analyte RNA–P-DNA hybrids. As a result, the ssDNA 5′-GGTCCACCAAACGTAATGCGGGGT-3′ was selected as a unique and complementary sequence of the SARS-CoV-2 genome featuring a length of 24 nucleotides and a high G/C content of 58%. This ssDNA was labelled with the fluorophore fluorescein amidite (FAM) at the 5’ end, a motif that gives green fluorescence at a wavelength of 518 nm. The resulting FAM–ssDNA strand is herein referred to as P-DNA. When the P-DNA is adsorbed by the MOF, electrons can be transferred from FAM to the MOF *via* PET to result into fluorescence quenching. Given the hydrophobic environment within the MOF pores we can assume intermolecular π-π-stacking interactions between the aromatic motifs of FAM and Me-IPA as dominating mechanism for PET.

The fabrication of the P-DNA@MOF platform was systematically explored as function of the P-DNA loading capacity with the overall goal to maximize P-DNA adsorption. These experiments were

performed by placing pristine MOF samples in nuclease free (NF) aqueous solutions of increasing concentration of P-DNA (125, 250, 375, 500, and 750 nM). After centrifugation, the respective supernatants were characterized by fluorescence spectroscopy for P-DNA content as a means for accurate quantification of P-DNA uptake within the MOF samples. As a result, a P-DNA saturation concentration of around 4 nmol/mg was determined by averaging the five samples (**Figure S3** and **Tables S2-3**). Further characterization of the P-DNA@MOF probes *via* SEM shows a similar morphology and particle size as comparted to the pristine MOF indicating no decomposition of the probe upon P-DNA loading (**Figure S4**).

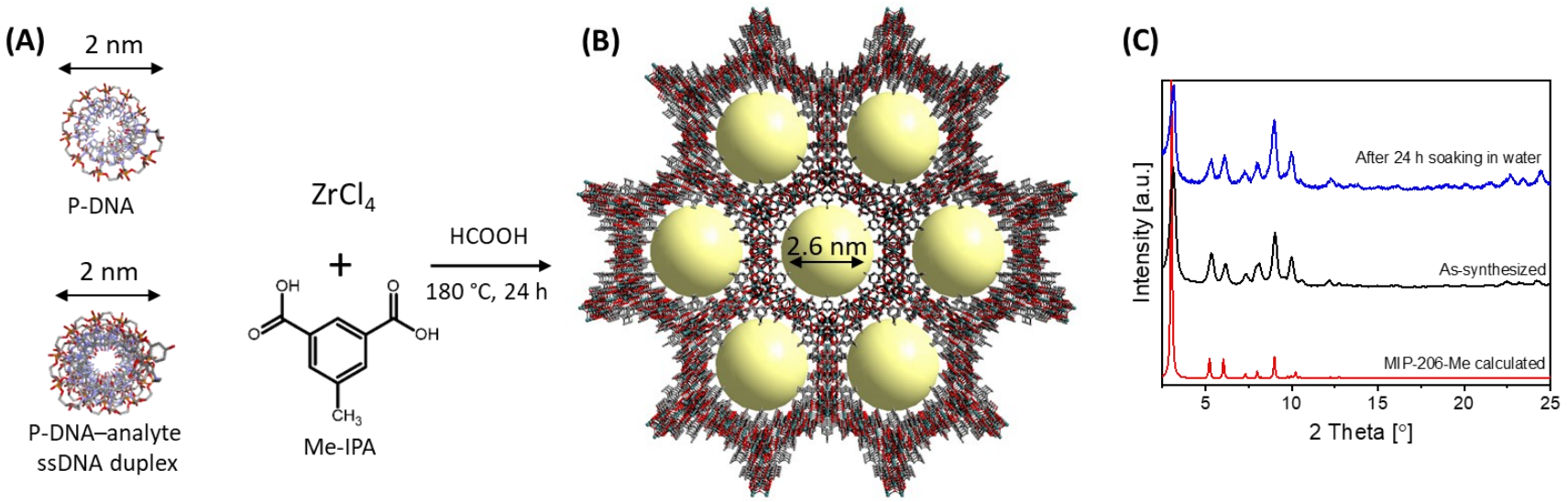

Figure 2. Demonstrating the viability of selected biosensor components. (A) Kinetic diameters of P-DNA and P-DNA–analyte ssDNA duplex; (B) synthesis scheme and packing diagram of MIP-206-Me along the crystallographic *c*-axis.; and (C) PXRD patterns of MIP-206-Me

Analyte detection validation through fluorescence regeneration testing. For this proof-of-concept study we choose to work with ssDNA analytes in lieu of RNA motifs given the superior stability and handleability of ssDNA *vs*. RNA.[46] Consequently, the ssDNA of composition 3'-ACCCCGCATTACGTTTGGTGGACC-5' was selected as representative analyte sequence of the SARS-CoV-2 genome. For simplicity, this analyte ssDNA is herein referred to as A-DNA. Introductory testing was performed to determine the fluorescence regeneration capability of the P-DNA@MOF probe as function of the P-DNA loading capacity and processing conditions, namely temperature and sonication. Two different P-DNA@MOF probes with P-DNA loading capacities of 1.5 and 3 nmol/mg were prepared as representative probes for low and high P-DNA loading scenarios, respectively. **Figure S5** shows a schematic representation of the probe fabrication methodology. An excess of A-DNA (2:1 ratio of A-DNA to P-DNA) was used for the regeneration testing to maximize the probability of A-DNA–P-DNA duplex formation and the resulting fluorescence signal. In addition, two different regeneration temperatures at either low (35 °C) or high (50 °C) temperature under sonication were explored to investigate the temperature dependency of the regeneration process. **Figure S6** shows a schematic representation of the regeneration testing methodology. As evident from **Figure 3A**, no fluorescence regeneration can be observed for the low P-DNA loading scenarios while the 3 nmol/mg P-DNA@MOF probe at 50 °C exhibits the most effective fluorescence regeneration. We thus decided to use fully saturated MOF probes under sonication at 50 °C moving forward.

In the next step we investigated the fluorescence regeneration efficiency with variation of the liquid phase. Per **Figure 3B**, 0.1 M Tris HCl buffer solution was found to be most effective resulting in an impressive 100-fold boosting of the fluorescence signal as compared to pure NF water as solution media. Stability testing revealed that the crystallinity of the MOF is not impacted under those regeneration conditions as evident from respective PXRD patterns before and after buffer exposure (**Figure S7**). Based on this finding we tested the limit of detection (LOD) in buffer solution using a P-DNA@MOF probe of 4 nmol/mg capacity. **Figure 3C** shows selected fluorescence regeneration signals as function of different A-DNA to loaded P-DNA ratios (2:1, 1:1, 1:200 and 1:2000). Notably, below the 1:1 ratio, signal changes are slight with varying A-DNA concentrations while above the 1:1 ratio an increased fluorescence signal is detected, displaying a non-linear relationship of regeneration compared to A-DNA concentration. However, given the perfectly flat control curve of pure buffer solution (no A-DNA added) combined with excellent calibration data (**Figure S8** and **Table S4**) we can conclude that the ratio at 1:2000 is the lowest experimentally determined LOD under given instrumental conditions. This ratio equates to an A-DNA concentration of 400 pM or 1.2×10^{11} copies/mL. Noteworthy, based on cost optimization, these parameters are obtained using only 0.1 mg of P-DNA@MOF probe in 2 mL of A-DNA solution. In addition to this quantitative analysis using fluorescence spectroscopy, a qualitative visible colorimetric change can be also

observed in the assay between the white colored unloaded MOF (**Figure 3E**), the yellow P-DNA@MOF probe (**Figure 3F**), and the probe after regeneration which shows the color diminishing towards the original white color indicating that P-DNA has been expelled from the MOF particles (**Figure 3G**). To the best of our knowledge, we found that this dual-signal readout capability is first of its kind among the pool of recent MOF-based viral RNA/DNA detection work[21–26].

Lastly, the selectivity of this detection platform was investigated using one random ssDNA sequence and four mutants where a defined nucleotide mismatch was placed at the 5' end (M1), the 3' end (M2), in the middle (M3), and three sequential mismatches in the middle of the oligomer (M4) with all mutants having the same sequence length of 24 nucleotides. **Table 1** lists an overview of these sequences and their respective mismatches with **Figure 3D** showing resulting fluorescence data from regeneration testing. Given that these selectivity experiments were performed under identical experimental conditions as described above for LOD testing, the scale of fluorescence intensity can be compared with data shown in **Figure 3C**. As a result, no meaningful fluorescence signal is observed from all mutants, however, M1 showed relatively a slightly higher signal than the other mutants, suggesting that a mutation at the mutant's 5' end which binds to the non-tagged 3' end of P-DNA had a much larger impact on the regeneration ability.

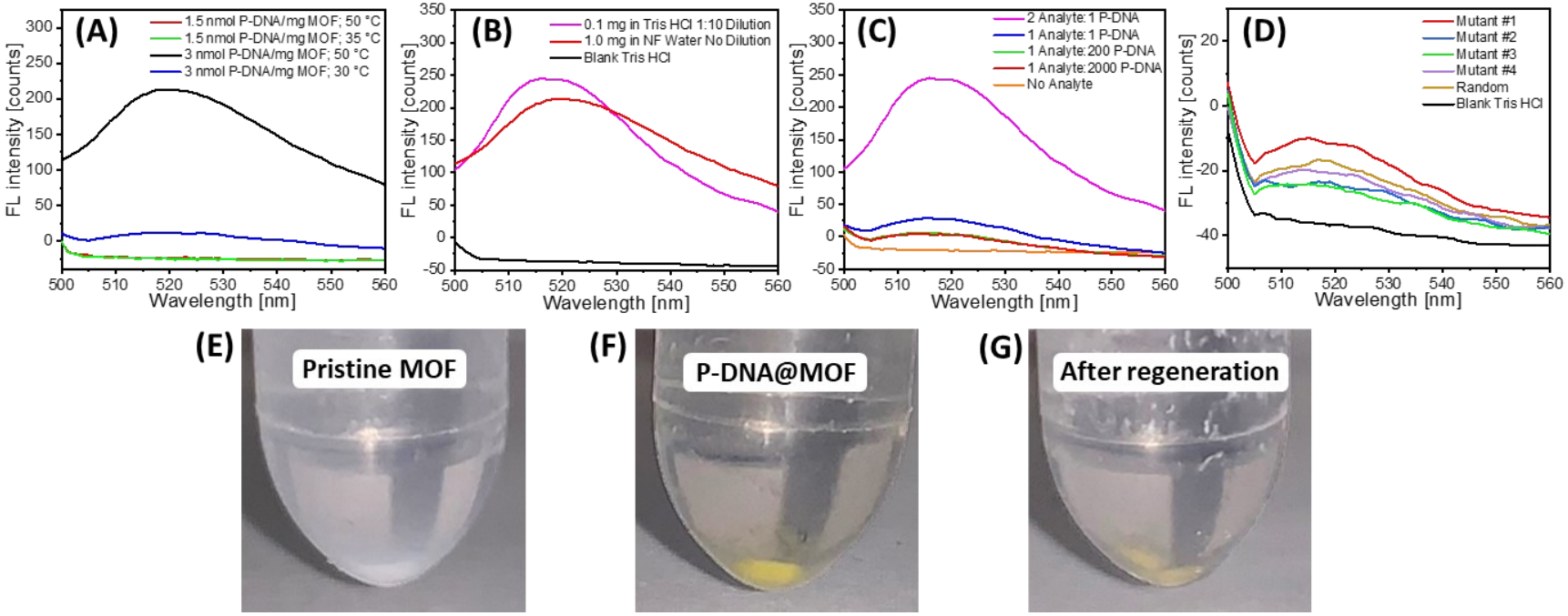

Figure 3. Systematic fluorescence regeneration testing. (A) Fluorescence regeneration with variation of temperature and P-DNA concentration in 1 mg MOF with constant 2:1 ratio of A-DNA to P-DNA in NF water demonstrating that higher P-DNA loadings and higher temperature facilitate the fluorescence regeneration process; (B) fluorescence regeneration with variation of the liquid phase demonstrating a boosting effect of Tris-HCl buffer as compared to NF water; (C) LOD testing with variation of A-DNA concentration at 50 °C with constant concentration of P-DNA in 0.1 mg MOF in Tris HCl buffer and control with no A-DNA added, diluted 1:10 before measuring; (D) selectivity testing with mutated A-DNA at 50 °C with constant concentration of P-DNA in 0.1 mg MOF sample and constant concentration of A-DNAs in 0.1 M Tris HCl buffer, diluted 1:10 before measuring; (E) photographs of the pristine MOF pellet, (F) P-DNA loaded MOF pellet, and (G) the MOF pellet after the regeneration process. All fluorescence data points were recorded with an excitation wavelength of 485 nm.

Table 1. Overview of oligonucleotide sequences used in this study. Mismatches as compared to the A-DNA are highlighted in red.

ssDNA Sequences																								
P-DNA (written 3'-5')	T	G	G	G	G	C	G	T	A	A	T	G	C	A	A	A	C	C	A	C	C	T	G	G	FAM
A-DNA	A	C	C	C	C	G	C	A	T	T	A	C	G	T	T	T	G	G	T	G	G	A	C	C	
Mutant #1	**T**	C	C	C	C	G	C	A	T	T	A	C	G	T	T	T	G	G	T	G	G	A	C	C	
Mutant #2	A	C	C	C	C	G	C	A	T	T	A	C	G	T	T	T	G	G	T	G	G	A	C	**G**	
Mutant #3	A	C	C	C	C	G	C	A	T	T	A	**G**	G	T	T	T	G	G	T	G	G	A	C	C	
Mutant #4	A	C	C	C	C	G	C	A	T	T	**T**	**G**	**C**	T	T	T	G	G	T	G	G	A	C	C	
Random	**G**	**T**	C	**A**	**T**	**A**	C	**T**	**G**	**G**	**C**	**A**	**T**	**A**	**C**	**G**	**A**	**T**	**C**	**T**	**T**	A	C	**T**	

Computational mechanistic investigations. The mechanism of A-DNA–P-DNA duplex formation and repulsion from the MOF pore was probed through classical computational methods in which the structures of P-DNA@MOF (**Figure 4A**), P-DNA (**Figure 4B**), and A-DNA–P-DNA duplex@MOF (**Figure 4C-D**) were modelled, the geometries optimized, and energies calculated. At first, these energy calculations demonstrate that the adsorption of P-DNA into the MOF pores is energetically favored since the total energy of the non-adsorbed P-DNA amounts a strongly positive value of 2648 kcal/mol while the P-DNA@MOF binding energy amounts a stable negative value of -1300 kcal/mol. Secondly, the strongly positive binding energy value of 2162 kcal/mol for the A-DNA–P-DNA duplex@MOF implies that the duplex formation inside the MOF pore is not energetically favored. This finding suggests that the duplex is formed outside of the pore potentially through a zipper-like mechanism. A schematic representation of this mechanism is shown in **Figure 4E** wherein the A-DNA removes the P-DNA from the pores at the MOF surface through duplex formation base pair by base pair, forming the duplex solely outside of the pores. This mechanism would also support the lack of full reversion of color change upon regeneration (**Figures 3E-G**) due to the limitation of surface-pore interactions, leaving P-DNA still adsorbed in the central pores of the MOF particles. In addition, binding energies of FAM@MOF (-32 kcal/mol), P-DNA@MOF (-1300 kcal/mol), and ssDNA@MOF (-1623 kcal/mol) where ssDNA@MOF is P-DNA@MOF without a FAM tag modification suggesting that the 3’ (unlabeled end) of the ssDNA preferentially enters the MOF pore before the FAM end. This finding supports the experimental results of the mutant testing showing that M1 having a mismatch at its 5’ end would still remove the P-DNA from the MOF pore as the duplex would mostly be formed outside of the pore already.

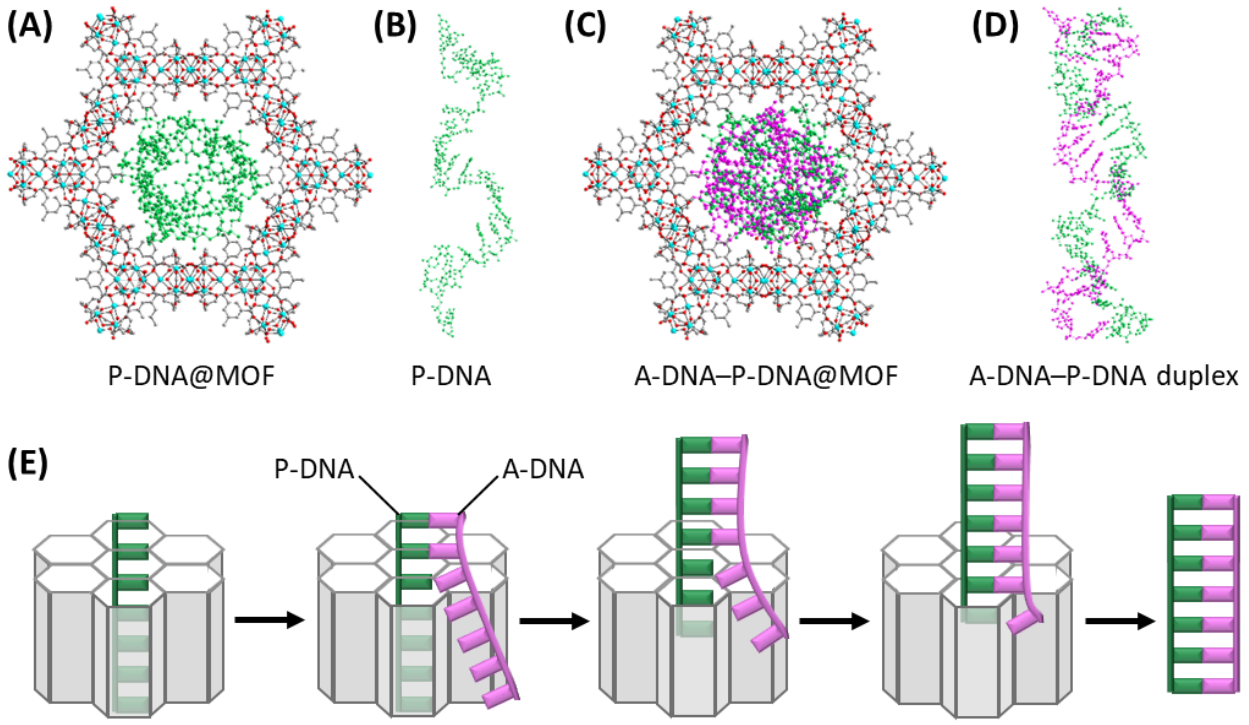

Figure 4. Simulated crystal structures of (A) P-DNA@MOF, (B) P-DNA, (C) A-DNA–P-DNA duplex@MOF, and (D) A-DNA-P-DNA duplex where P-DNA is colored green and A-DNA is colored pink; and (E) schematic representation of the proposed zipper-like mechanism of A-DNA (pink) removing P-DNA (green) from the MOF pore by forming a A-DNA–P-DNA duplex through base pairing.

Conclusions

In this proof-of-concept study we are expanding the application range of MOFs by reporting on a novel P-DNA@MOF biosensor which has the capability to detect genetic material of the SARS-CoV-2 genome. We show that this detection process features dual-signal readout capability, namely, quantitative fluorescent assessment with LOD of 400 pM coupled with qualitative visual colorimetric sensing. It is envisioned that the sensitivity of this process can be further improved by increasing the mass of P-DNA@MOF per analyte volume and/or the combination with PCR amplification methods.[47] In addition, through comprehensive mutant testing we demonstrate ultra-high selectivity of the detection process down to a single-base mismatch within the nucleotide sequences of the analyte. The cost for this detection platform is estimated around 3 USD per MOF probe unit (0.1 mg) making it competitive for commercialization. Eventually, this work is expected to inspire further research as the method has the potential to be expanded toward the design of more sophisticated multi-probe detection platforms, for example, through the co-adsorption of P-DNAs antisense to viral genomes of different SARS-CoV-2 variants and/or the common flu which each possesses a unique fluorophore tag. In summary, we herein present a novel MOF-based diagnostic platform

featuring (i) remarkable detection performances including picomolar target sensitivities and single-base mismatch selectivities; (ii) low-cost, simple instrumentation, and rapid detection characteristics; and (iii) simple adaptability to new variants—all important milestones to move the field toward the development of reliable molecular point-of-care tests.

Experimental Section

Materials. All chemicals were used as purchased without further purification unless specifically noted. 5-methylisophthalic acid hydrate was obtained from Chem Impex, $ZrCl_4$ from Strem Chemicals Inc., formic acid from Sigma-Aldrich, molecular biology grade sterile water from Ricca, and custom ssDNA and FAM-labelled-ssDNA solutions from ThermoFisher Scientific.

MOF synthesis. MIP-206-Me was synthesized as previously reported.[34] Briefly, 1.1 g (6.6 mmol) of 5-methyl isophthalic acid was placed with 5 mL of formic acid in a 25 mL Teflon cup followed by sonication at room temperature for 5 min. 2 g (8.6 mmol) of $ZrCl_4$ was added to the mixture followed by sonication for another 10 minutes. The Teflon cup was sealed in a steel autoclave and heated at 180 °C for 24 h. The reaction product was filtered by vacuum filtration and washed with acetone before being air-dried.

P-DNA@MOF fabrication. 1 mg MOF samples were prepared by weighing 1 mg samples of as-synthesized MIP-206-Me into 2 mL nuclease free (NF) Eppendorf tubes. The tubes were then filled to the 2 mL line with NF water, shaken, and centrifuged before carefully removing the water above the MOF pellet using an NF needle and syringe. This process of washing the MOF was repeated twice more to ensure that the pores were washed clean of any guests which could harm the P-DNA. A corresponding amount of P-DNA in NF water was added to the tube and shaken before being centrifuged at 10 °C. The head solution was removed with an NF needle and syringe leaving a yellow pellet. The tube was then refilled with NF water and shaken before being centrifuged at 10 °C and the head solution removed again to remove any non-adsorbed P-DNA from the tube.

Sub-1 mg samples were prepared by grinding the as-synthesized MIP-206-Me powder using a mortar and pestle into a finer powder. 20 mg of the finely powdered MOF was placed in a 50 mL NF tube to which 20 mL of 200 proof ethanol was added. The tube was sonicated in a bath and appropriate aliquots of the dispersion (e.g., 0.1 mL for 0.1 mg test) were placed in 2 mL NF Eppendorf tubes. The tubes were then filled with NF water to a total volume of 2 mL, shaken, and centrifuged before carefully removing the supernatant above the MOF pellet using an NF needle and syringe. This process of washing the MOF was repeated twice more to ensure that the pores were washed clean of ethanol and any guests which could harm the P-DNA. An amount of NF water was added to the tube and the pellet redispersed by sonication before

adding the corresponding amount of P-DNA to achieve the desired P-DNA concentration before being centrifuged at 10 °C. The head solution was removed with an NF needle and syringe leaving a small yellow pellet. The tube was then refilled with NF water and shaken before being centrifuged at 10 °C and the supernatant removed again to remove any non-adsorbed P-DNA from the tube.

P-DNA loading quantification. The MOF was processed as described above followed by adding P-DNA in various concentrations (125, 250, 375, 500, 750, and 1000 nM) before being centrifuged at 10 °C. About 1.5 mL of the head solution was removed with a NF needle and syringe, the needle was then removed from the syringe and replaced with a 0.1 μm syringe filter. The solution was pushed through the filter into a 1.4 mL capacity fluorimeter cell and an emission spectrum collected with an excitation wavelength of 485 nm.

Fluorescence regeneration testing. P-DNA@MOF sample in an Eppendorf tube which has been washed as described above was filled with an amount of NF water and an amount of buffer solution then briefly sonicated to redisperse the P-DNA@MOF pellet before adding the desired amount of A-DNA, giving a final buffer concentration of wither 0 M or 0.1 M with varying A-DNA concentrations depending on the sample. The tube was then placed through a thin piece of Styrofoam so that the bottom is sticking out and sonicated in a sonication bath with controlled temperature for 30 minutes. After centrifugation at 10 °C, about 1.5 mL of the head solution was removed with an NF needle and syringe, the needle was then removed from the syringe and replaced with a 0.1 μm syringe filter. The solution was pushed through the filter into either a 1.4 mL capacity fluorimeter cell and an emission spectrum collected with an excitation wavelength of 485 nm (for samples without buffer) or an unused NF Eppendorf tube before being further diluted in a 1:10 ratio with NF buffer solution before being pipetted into a 1.4 mL capacity fluorimeter cell and an emission spectrum collected with an excitation wavelength of 485 nm.

Powder X-ray diffraction. PXRD data of as-synthesized MIP-206-Me was collected on a Bruker D2 Phaser diffractometer with a sealed Cu tube (λ = 1.54178 Å) where the powder was dispersed on a low-background Si wafer disc for analysis.

Fluorescence spectrophotometry. Fluorescence measurements were recorded using a Varian Cary Eclipse Fluorescence Spectrophotometer with a semi-micro quartz fluorimeter cuvette obtained from Starna cells.

Computational Methods. The pristine MOF structure was initially optimized by density functional theory (DFT) using the Quickstep[48] code of the CP2K 8.1 package with periodic boundary conditions. Perdew−Burke−Ernzerhof (PBE)[49] exchange-correlation functional was used for the energy minimization,

employing GTH pseudopotentials, DZVP-MOLOPT-SR-GTH contracted Gaussian basis sets, and an auxiliary plane wave basis set. The plane wave's cutoff was set to 660 Ry and it was mapped on a 5-level multigrid with a relative cutoff of 60 Ry. The pre-optimized MOF was then used as the host to encapsulate the ssDNA. The geometry of the pristine ssDNA, P-DNA, and the A-DNA–P-DNA duplex were constructed using 24 DNA equivalent sequences and the pre-optimized FAM-structure followed by energy minimization scans were performed using the Forcite module of Material Studio 2020.1.0.5.[50] The Universal force field was used for the optimization process with Smart algorithm and current charges. Ewald summation method was used with an accuracy 0.0001 kcal/mol, and a long-range van der Waals correction was also included in the energy minimization scans. The optimized ssDNA, P-DNA, and the A-DNA–P-DNA duplex structures were then infiltrated into the pre-optimized MOF, and the resulted composites were geometry optimized using Forcite module with same level of theory used in the ssDNA optimization processes whereas the MOF geometry was constrained. The binding energy (BE) was calculated using the equation $BE = E_{Composite} - (E_{MOF} + E_{DNA})$ while this equation was modified in the duplex@MOF calculation as follows $BE = E_{Duplex@MOF} - (E_{MOF} + BE_{Duplex})$, whereas the BE_{Duplex} addresses the interaction between the ssDNA helices.[51]

Supporting Information

Overview of previous work in viral genetic material sensing using MOFs, solid-state UV-Visible spectrum of pristine MOF, SEM images of pristine MOF and P-DNA@MOF, calibration curve data of P-DNA in NF water and Tris HCl buffer, P-DNA saturation of MOF data, schematic representations of test fabrication and testing procedure, PXRD of sample after treatment with Tris HCl buffer.

Acknowledgements

M.W. gratefully acknowledges the U.S. National Science Foundation CAREER Program (award no. DMR-1752771) and Clarkson's 2022 Center for Advanced Materials Characterization (CAMP) Graduate Research Fellowship Program for support of this work. J.D. thanks the McNair scholar program under the umbrella of the Community of Underrepresented Professional Opportunities (CUPO) at Clarkson University.

Author Contributions

M.W. conceived and designed the idea of the project. M.W. and J.H. designed the experiments. J.H. synthesized materials and collected and analyzed the data. J.D., Z.G., and S.D. assisted with the experiments and characterizations. M.J. performed computations and analyzed computational results. P.K. and T.L.

selected and handled biological agents for experiments. J.H. and M.W. prepared the manuscript and all authors contributed to the final version.

References

(1) Hsiao, T.-C.; Chuang, H.-C.; Griffith, S. M.; Chen, S.-J.; Young, L.-H. COVID-19: An Aerosol's Point of View from Expiration to Transmission to Viral-Mechanism. *Aerosol Air Qual. Res.* **2020**, *20* (5), 905–910. https://doi.org/10.4209/aaqr.2020.04.0154.

(2) Shereen, M. A.; Khan, S.; Kazmi, A.; Bashir, N.; Siddique, R. COVID-19 Infection: Origin, Transmission, and Characteristics of Human Coronaviruses. *J. Adv. Res.* **2020**, *24*, 91–98. https://doi.org/10.1016/j.jare.2020.03.005.

(3) Peng, X.; Xu, X.; Li, Y.; Cheng, L.; Zhou, X.; Ren, B. Transmission Routes of 2019-NCoV and Controls in Dental Practice. *Int. J. Oral Sci.* **2020**, *12* (1), 9. https://doi.org/10.1038/s41368-020-0075-9.

(4) Benda, A.; Zerajic, L.; Ankita, A.; Cleary, E.; Park, Y.; Pandey, S. COVID-19 Testing and Diagnostics: A Review of Commercialized Technologies for Cost, Convenience and Quality of Tests. *Sensors* **2021**, *21* (19), 6581. https://doi.org/10.3390/s21196581.

(5) Manabe, Y. C.; Sharfstein, J. S.; Armstrong, K. The Need for and Limits of More and Better Testing for COVID-19. *JAMA* **2020**, *324* (21), 2153–2154. https://doi.org/10.1001/jama.2020.21694.

(6) De Felice, M.; De Falco, M.; Zappi, D.; Antonacci, A.; Scognamiglio, V. Isothermal Amplification-Assisted Diagnostics for COVID-19. *Biosens. Bioelectron.* **2022**, *205*, 114101. https://doi.org/10.1016/j.bios.2022.114101.

(7) Kyosei, Y.; Yamura, S.; Namba, M.; Yoshimura, T.; Watabe, S.; Ito, E. Antigen Tests for COVID-19. *Biophys. Physicobiology* **2021**, *18*, 28–39. https://doi.org/10.2142/biophysico.bppb-v18.004.

(8) Rasmi, Y.; Li, X.; Khan, J.; Ozer, T.; Choi, J. R. Emerging Point-of-Care Biosensors for Rapid Diagnosis of COVID-19: Current Progress, Challenges, and Future Prospects. *Anal. Bioanal. Chem.* **2021**, *413* (16), 4137–4159. https://doi.org/10.1007/s00216-021-03377-6.

(9) Corman, V. M.; Landt, O.; Kaiser, M.; Molenkamp, R.; Meijer, A.; Chu, D. K.; Bleicker, T.; Brünink, S.; Schneider, J.; Schmidt, M. L.; Mulders, D. G.; Haagmans, B. L.; van der Veer, B.; van den Brink, S.; Wijsman, L.; Goderski, G.; Romette, J.-L.; Ellis, J.; Zambon, M.; Peiris, M.; Goossens, H.; Reusken, C.; Koopmans, M. P.; Drosten, C. Detection of 2019 Novel Coronavirus (2019-NCoV) by Real-Time RT-PCR. *Eurosurveillance* **2020**, *25* (3), 2000045. https://doi.org/10.2807/1560-7917.ES.2020.25.3.2000045.

(10) Jayakody, H.; Rowland, D.; Pereira, C.; Blackwell, R.; Lasota, T.; Laverick, M.; Tisi, L.; Leese, H. S.; Walsham, A. D. S. Development of a High Sensitivity RT-PCR Assay for Detection of SARS-CoV-2 in Individual and Pooled Nasopharyngeal Samples. *Sci. Rep.* **2022**, *12* (1), 5369. https://doi.org/10.1038/s41598-022-09254-1.

(11) Amaral, C.; Antunes, W.; Moe, E.; Duarte, A. G.; Lima, L. M. P.; Santos, C.; Gomes, I. L.; Afonso, G. S.; Vieira, R.; Teles, H. S. S.; Reis, M. S.; da Silva, M. A. R.; Henriques, A. M.; Fevereiro, M.; Ventura, M. R.; Serrano, M.; Pimentel, C. A Molecular Test Based on RT-LAMP for Rapid, Sensitive and Inexpensive Colorimetric Detection of SARS-CoV-2 in Clinical Samples. *Sci. Rep.* **2021**, *11* (1), 16430. https://doi.org/10.1038/s41598-021-95799-6.

(12) Kepczynski, C. M.; Genigeski, J. A.; Koski, R. R.; Bernknopf, A. C.; Konieczny, A. M.; Klepser, M. E. A Systematic Review Comparing At-Home Diagnostic Tests for SARS-CoV-2: Key Points for Pharmacy Practice, Including Regulatory Information. *J. Am. Pharm. Assoc.* **2021**, *61* (6), 666-677.e2. https://doi.org/10.1016/j.japh.2021.06.012.

(13) Mercer, T. R.; Salit, M. Testing at Scale during the COVID-19 Pandemic. *Nat. Rev. Genet.* **2021**, *22* (7), 415–426. https://doi.org/10.1038/s41576-021-00360-w.

(14) Choi, J. R. Development of Point-of-Care Biosensors for COVID-19. *Front. Chem.* **2020**, *8*.
(15) Pinheiro, T.; Cardoso, A. R.; Sousa, C. E. A.; Marques, A. C.; Tavares, A. P. M.; Matos, A. M.; Cruz, M. T.; Moreira, F. T. C.; Martins, R.; Fortunato, E.; Sales, M. G. F. Paper-Based Biosensors for COVID-19: A Review of Innovative Tools for Controlling the Pandemic. *ACS Omega* **2021**, *6* (44), 29268–29290. https://doi.org/10.1021/acsomega.1c04012.
(16) Kirchon, A.; Feng, L.; Drake, H. F.; Joseph, E. A.; Zhou, H.-C. From Fundamentals to Applications: A Toolbox for Robust and Multifunctional MOF Materials. *Chem. Soc. Rev.* **2018**, *47* (23), 8611–8638. https://doi.org/10.1039/C8CS00688A.
(17) Li, H.; Wang, K.; Sun, Y.; Lollar, C. T.; Li, J.; Zhou, H.-C. Recent Advances in Gas Storage and Separation Using Metal–Organic Frameworks. *Mater. Today* **2018**, *21* (2), 108–121. https://doi.org/10.1016/j.mattod.2017.07.006.
(18) Zhang, Y.; Yuan, S.; Day, G.; Wang, X.; Yang, X.; Zhou, H.-C. Luminescent Sensors Based on Metal-Organic Frameworks. *Coord. Chem. Rev.* **2018**, *354*, 28–45. https://doi.org/10.1016/j.ccr.2017.06.007.
(19) Zhang, Q.; Wang, C.-F.; Lv, Y.-K. Luminescent Switch Sensors for the Detection of Biomolecules Based on Metal–Organic Frameworks. *Analyst* **2018**, *143* (18), 4221–4229. https://doi.org/10.1039/C8AN00816G.
(20) Bao, G.; Rhee, W. J.; Tsourkas, A. Fluorescent Probes for Live-Cell RNA Detection. *Annu. Rev. Biomed. Eng.* **2009**, *11* (1), 25–47. https://doi.org/10.1146/annurev-bioeng-061008-124920.
(21) Qin, L.; Lin, L.-X.; Fang, Z.-P.; Yang, S.-P.; Qui, G.-H.; Chen, J.-X.; Chen, W.-H. A Water-Stable Metal–Organic Framework of a Zwitterionic Carboxylate with Dysprosium: A Sensing Platform for Ebolavirus RNA Sequences - Chemical Communications (RSC Publishing). *Chem. Commun.* **2016**, *21* (1), 132–135. https://doi.org/10.1039/c5cc06697b.
(22) Qiu, G.-H.; Weng, Z.-H.; Hu, P.-P.; Duan, W.-J.; Xie, B.-P.; Sun, B.; Tang, X.-Y.; Chen, J.-X. Synchronous Detection of Ebolavirus Conserved RNA Sequences and Ebolavirus-Encoded MiRNA-like Fragment Based on a Zwitterionic Copper (II) Metal–Organic Framework. *Talanta* **2018**, *180*, 396–402. https://doi.org/10.1016/j.talanta.2017.12.045.
(23) Yang, S.-P.; Chen, S.-R.; Liu, S.-W.; Tang, X.-Y.; Qin, L.; Qiu, G.-H.; Chen, J.-X.; Chen, W.-H. Platforms Formed from a Three-Dimensional Cu-Based Zwitterionic Metal–Organic Framework and Probe Ss-DNA: Selective Fluorescent Biosensors for Human Immunodeficiency Virus 1 Ds-DNA and Sudan Virus RNA Sequences. *Anal. Chem.* **2015**, *87* (24), 12206–12214. https://doi.org/10.1021/acs.analchem.5b03084.
(24) Sun, B.; Zhao, H.-Q.; Xie, B.-P.; Bai, L.-P.; Jiang, Z.-H.; Chen, J.-X. Sequence-Specific Fluorometric Recognition of HIV-1 Ds-DNA with Zwitterionic Zinc(II)-Carboxylate Polymers. *J. Inorg. Biochem.* **2017**, *176*, 17–23. https://doi.org/10.1016/j.jinorgbio.2017.07.024.
(25) Yang, S.-P.; Zhao, W.; Hu, P.-P.; Wu, K.-Y.; Jiang, Z.-H.; Bai, L.-P.; Li, M.-M.; Chen, J.-X. Lanthanum-Based Metal–Organic Frameworks for Specific Detection of Sudan Virus RNA Conservative Sequences down to Single-Base Mismatch. *Inorg. Chem.* **2017**, *56* (24), 14880–14887. https://doi.org/10.1021/acs.inorgchem.7b02107.
(26) Xie, B.-P.; Qiu, G.-H.; Hu, P.-P.; Liang, Z.; Liang, Y.-M.; Sun, B.; Bai, L.-P.; Jiang, Z.-H.; Chen, J.-X. Simultaneous Detection of Dengue and Zika Virus RNA Sequences with a Three-Dimensional Cu-Based Zwitterionic Metal–Organic Framework, Comparison of Single and Synchronous Fluorescence Analysis. *Sens. Actuators B Chem.* **2018**, *254*, 1133–1140. https://doi.org/10.1016/j.snb.2017.06.085.
(27) Figueira, F.; S. Barbosa, J.; F. Mendes, R.; S. Braga, S.; A. Almeida Paz, F. Virus Meet Metal-Organic Frameworks: A Nanoporous Solution to a World-Sized Problem? *Mater. Today* **2021**, *43*, 84–98. https://doi.org/10.1016/j.mattod.2020.10.024.
(28) Wang, Y.; Hu, Y.; He, Q.; Yan, J.; Xiong, H.; Wen, N.; Cai, S.; Peng, D.; Liu, Y.; Liu, Z. Metal-Organic Frameworks for Virus Detection. *Biosens. Bioelectron.* **2020**, *169*, 112604. https://doi.org/10.1016/j.bios.2020.112604.

(29) Sheta, S. M.; El-Sheikh, S. M. Nanomaterials and Metal-Organic Frameworks for Biosensing Applications of Mutations of the Emerging Viruses. *Anal. Biochem.* **2022**, *648*, 114680. https://doi.org/10.1016/j.ab.2022.114680.
(30) Udourioh, G. A.; Solomon, M. M.; Epelle, E. I. Metal Organic Frameworks as Biosensing Materials for COVID-19. *Cell. Mol. Bioeng.* **2021**, *14* (6), 535–553. https://doi.org/10.1007/s12195-021-00686-9.
(31) Pandey, M. D. Luminescent Metal–Organic Frameworks as Biosensors. *Mater. Lett.* **2022**, *308*, 131230. https://doi.org/10.1016/j.matlet.2021.131230.
(32) Almasi, M. A Review on State of Art and Perspectives of Metal-Organic Frameworks (MOFs) in the Fight against Coronavirus SARS-CoV-2: Journal of Coordination Chemistry: Vol 74, No 13. *J. Coord. Chem.* **2021**, *74* (13), 2111–2127. https://doi.org/10.1080/009589722.2021.1965130.
(33) Ali, G. K.; Omer, K. M. Nanozyme and Stimulated Fluorescent Cu-Based Metal–Organic Frameworks (Cu-MOFs) Functionalized with Engineered Aptamers as a Molecular Recognition Element for Thrombin Detection in the Plasma of COVID-19 Patients. *ACS Omega* **2022**, *7* (41), 36804–36810. https://doi.org/10.1021/acsomega.2c05232.
(34) Reyes, S.; Rizzo, E.; Ting, A.; Dikici, E.; Daunert, S.; Deo, S. K. Metal Organic Framework Encapsulated Tamavidin-Gluc Reporter: Application in COVID-19 Spike Antigen Bioluminescent Immunoassay. *Sens. Diagn.* **2022**, *1* (6), 1198–1208. https://doi.org/10.1039/D2SD00145D.
(35) Yodsin, N.; Sriphumrat, K.; Mano, P.; Kongpatpanich, K.; Namuangruk, S. Metal-Organic Framework MIL-100(Fe) as a Promising Sensor for COVID-19 Biomarkers Detection. *Microporous Mesoporous Mater.* **2022**, *343*, 112187. https://doi.org/10.1016/j.micromeso.2022.112187.
(36) Rabiee, N.; Fatahi, Y.; Ahmadi, S.; Abbariki, N.; Ojaghi, A.; Rabiee, M.; Radmanesh, F.; Dinarvand, R.; Bagherzadeh, M.; Mostafavi, E.; Ashrafizadeh, M.; Makvandi, P.; Lima, E. C.; Saeb, M. R. Bioactive Hybrid Metal-Organic Framework (MOF)-Based Nanosensors for Optical Detection of Recombinant SARS-CoV-2 Spike Antigen. *Sci. Total Environ.* **2022**, *825*, 153902. https://doi.org/10.1016/j.scitotenv.2022.153902.
(37) Jiang, Z. W.; Zhao, T. T.; Li, C. M.; Li, Y. F.; Huang, C. Z. 2D MOF-Based Photoelectrochemical Aptasensor for SARS-CoV-2 Spike Glycoprotein Detection. *ACS Appl. Mater. Interfaces* **2021**, *13* (42), 49754–49761. https://doi.org/10.1021/acsami.1c17574.
(38) Xie, B.; Yan, Y.; Wu, J.; Cai, X.; Zheng, J.; Lan, Y.; Tang, X.; Fan, J.; Zheng, S.; Cai, S. Three-Component Covalent Organic Framework Nanosheets for the Detection of MicroRNAs. *Crystals* **2022**, *12* (11), 1628. https://doi.org/10.3390/cryst12111628.
(39) Aulakh, D.; Liu, L.; Varghese, J. R.; Xie, H.; Islamoglu, T.; Duell, K.; Kung, C.-W.; Hsiung, C.-E.; Zhang, Y.; Drout, R. J.; Farha, O. K.; Dunbar, K. R.; Han, Y.; Wriedt, M. Direct Imaging of Isolated Single-Molecule Magnets in Metal–Organic Frameworks. *J. Am. Chem. Soc.* **2019**, *141* (7), 2997–3005. https://doi.org/10.1021/jacs.8b11374.
(40) Aulakh, D.; Pyser, J. B.; Zhang, X.; Yakovenko, A. A.; Dunbar, K. R.; Wriedt, M. Metal–Organic Frameworks as Platforms for the Controlled Nanostructuring of Single-Molecule Magnets. *J. Am. Chem. Soc.* **2015**, *137* (29), 9254–9257. https://doi.org/10.1021/jacs.5b06002.
(41) Aulakh, D.; Bilan, H. K.; Wriedt, M. Porous Substrates as Platforms for the Nanostructuring of Molecular Magnets. *CrystEngComm* **2018**, *20* (8), 1011–1030. https://doi.org/10.1039/C7CE01978E.
(42) Aulakh, D.; Xie, H.; Shen, Z.; Harley, A.; Zhang, X.; Yakovenko, A. A.; Dunbar, K. R.; Wriedt, M. Systematic Investigation of Controlled Nanostructuring of Mn12 Single-Molecule Magnets Templated by Metal–Organic Frameworks. *Inorg. Chem.* **2017**, *56* (12), 6965–6972. https://doi.org/10.1021/acs.inorgchem.7b00514.
(43) Peng, S.; Bie, B.; Sun, Y.; Liu, M.; Cong, H.; Zhou, W.; Xia, Y.; Tang, H.; Deng, H.; Zhou, X. Metal-Organic Frameworks for Precise Inclusion of Single-Stranded DNA and Transfection in Immune Cells. *Nat. Commun.* **2018**, *9* (1), 1293. https://doi.org/10.1038/s41467-018-03650-w.

(44) Wang, S.; Chen, L.; Wahiduzzaman, M.; Tissot, A.; Zhou, L.; Ibarra, I. A.; Gutiérrez-Alejandre, A.; Lee, J. S.; Chang, J.-S.; Liu, Z.; Marrot, J.; Shepard, W.; Maurin, G.; Xu, Q.; Serre, C. A Mesoporous Zirconium-Isophthalate Multifunctional Platform. *Matter* **2021**, *4* (1), 182–194. https://doi.org/10.1016/j.matt.2020.10.009.
(45) CDC. Research Use Only 2019-Novel Coronavirus (2019-NCoV) Real-Time RT-PCR Primers and Probes, 2020. https://www.cdc.gov/coronavirus/2019-ncov/lab/rt-pcr-panel-primer-probes.html (accessed 2022-04-11).
(46) Roberts, R. W.; Crothers, D. M. Stability and Properties of Double and Triple Helices: Dramatic Effects of RNA or DNA Backbone Composition. *Science* **1992**, *258* (5087), 1463–1466. https://doi.org/10.1126/science.1279808.
(47) Wozniak, A.; Cerda, A.; Ibarra-Henríquez, C.; Sebastian, V.; Armijo, G.; Lamig, L.; Miranda, C.; Lagos, M.; Solari, S.; Guzmán, A. M.; Quiroga, T.; Hitschfeld, S.; Riveras, E.; Ferrés, M.; Gutiérrez, R. A.; García, P. A Simple RNA Preparation Method for SARS-CoV-2 Detection by RT-QPCR. *Sci. Rep.* **2020**, *10* (1), 16608. https://doi.org/10.1038/s41598-020-73616-w.
(48) Kühne, T. D.; Iannuzzi, M.; Del Ben, M.; Rybkin, V. V.; Seewald, P.; Stein, F.; Laino, T.; Khaliullin, R. Z.; Schütt, O.; Schiffmann, F.; Golze, D.; Wilhelm, J.; Chulkov, S.; Bani-Hashemian, M. H.; Weber, V.; Borštnik, U.; Taillefumier, M.; Jakobovits, A. S.; Lazzaro, A.; Pabst, H.; Müller, T.; Schade, R.; Guidon, M.; Andermatt, S.; Holmberg, N.; Schenter, G. K.; Hehn, A.; Bussy, A.; Belleflamme, F.; Tabacchi, G.; Glöß, A.; Lass, M.; Bethune, I.; Mundy, C. J.; Plessl, C.; Watkins, M.; VandeVondele, J.; Krack, M.; Hutter, J. CP2K: An Electronic Structure and Molecular Dynamics Software Package - Quickstep: Efficient and Accurate Electronic Structure Calculations. *J. Chem. Phys.* **2020**, 194103 (47 pp.). https://doi.org/10.1063/5.0007045.
(49) Perdew, J. P.; Burke, K.; Ernzerhof, M. Generalized Gradient Approximation Made Simple. *Phys. Rev. Lett.* **1996**, *77* (18), 3865–3868. https://doi.org/10.1103/PhysRevLett.77.3865.
(50) BIOVIA Materials Studio - BIOVIA - Dassault Systèmes®, 2020. https://www.3ds.com/products-services/biovia/products/molecular-modeling-simulation/biovia-materials-studio/ (accessed 2022-08-01).
(51) You, W.; Liu, Y.; Howe, J. D.; Sholl, D. S. Competitive Binding of Ethylene, Water, and Carbon Monoxide in Metal–Organic Framework Materials with Open Cu Sites. *J. Phys. Chem. C* **2018**, *122* (16), 8960–8966. https://doi.org/10.1021/acs.jpcc.8b00909.

TOC image